International Journal of Nanomedicine Dovepress

Open Access Full Text Article ORIGINAL RESEARCH

Tracing Sentinel Lymph Nodes and Inhibiting Lymphatic Metastasis with TiN Nanobipyramids Through Photothermal Therapy

Yan-Neng Xu[1,*], Xiaopeng Bai[2,*], Jian-Li Chen[3,*], Xuan Wu[1], Dan Yin[1], Gang Yuan[1], Rongyang Dai[4], Xiao-Ming Zhu[1,5], Jianfang Wang[2]

[1]State Key Laboratory of Quality Research in Chinese Medicines, Macau Institute for Applied Research in Medicine and Health, Macau University of Science and Technology, Taipa, Macau SAR, 999078, People's Republic of China; [2]Department of Physics, The Chinese University of Hong Kong, Shatin, Hong Kong SAR, 999077, People's Republic of China; [3]Modern Research Center for Traditional Chinese Medicine, Shanxi University, Taiyuan, Shanxi, 030006, People's Republic of China; [4]Department of Biochemistry and Molecular Biology, Southwest Medical University, Luzhou, Sichuan, 646000, People's Republic of China; [5]Zhuhai MUST Science and Technology Research Institute, Macau University of Science and Technology, Zhuhai, Guangdong, 519099, People's Republic of China

*These authors contributed equally to this work

Correspondence: Xiao-Ming Zhu, State Key Laboratory of Quality Research in Chinese Medicines, Macau Institute for Applied Research in Medicine and Health, Macau University of Science and Technology, Taipa, Macau SAR, 999078, People's Republic of China, Email xmzhu@must.edu.mo; Jianfang Wang, Department of Physics, The Chinese University of Hong Kong, Shatin, Hong Kong SAR, 999077, People's Republic of China, Email jfwang@phy.cuhk.edu.hk

Background: The lymphatic system is the major route of cancer metastasis, and sentinel lymph nodes (SLNs) are the first station for the spread of cancer cells. Accurate identification of SLNs by tracers during surgery is crucial for SLN biopsy and lymphadenectomy. However, conventional monomodal tracers such as blue dyes and carbon nanoparticles often induce a misjudgment of SLNs and thus are still unsatisfying for clinical applications. In addition, SLN imaging agents with therapeutic capabilities to achieve perfect theranostics have been less exploited.

Purpose: Titanium nitride (TiN) nanostructures have the advantages of high stability and low cost and show superior plasmonic properties over both the visible and near-infrared (NIR) regions. Herein we report on the synthesis of TiN nanobipyramids (NBPs) with large sizes for multimodal SLN mapping.

Methods: A hydrothermal method and post nitridation treatment were used to prepare the TiN NBPs. Bright- and dark-field imaging of SLNs with TiN NBPs were performed. The effect of TiN NBP size on SLN tracing was studied. The effect of TiN NBP-based photothermal ablation of SLNs combined with removal of primary tumors on pulmonary metastasis was studied.

Results: The TiN NBPs with dual bright- and dark-field imaging functions show high drainage in lymph nodes and thus can act as a potential substitute for SLN tracing. Moreover, owing to the superior plasmonic properties of TiN nanostructures, the produced TiN NBPs show a high photothermal conversion efficiency under 1064 nm laser irradiation. TiN NBP-based photothermal ablation of metastatic LNs in the second NIR window (NIR-II) combined with surgical removal of primary tumors shows remarkable inhibition of pulmonary metastasis.

Conclusion: This study not only demonstrates TiN NBPs as a new tracer for SLN mapping, but also presents a strategy for the photothermal ablation of lymph nodes in NIR-II for the inhibition of lymphatic metastasis.

Keywords: TiN nanobipyramids, sentinel lymph nodes, lymph node mapping, photothermal therapy, second near-infrared window

Introduction

Cancer metastasis is hard to eliminate with conventional surgery, chemotherapy, and radiation. It is directly or indirectly responsible for more than 90% of human cancer deaths.[1] Precise identification and effective block of metastasis to prevent distant invasion are of great importance in cancer therapy. The lymphatic system is the main route for the spread of cancer cells.[2] During lymphatic metastasis, sentinel lymph nodes (SLNs) are the initial target organs of cancer cells

Received: 24 July 2024
Accepted: 13 December 2024
Published: 19 December 2024

© 2024 Xu et al. This work is published and licensed by Dove Medical Press Limited. The full terms of this license are available at https://www.dovepress.com/terms.php and incorporate the Creative Commons Attribution – Non Commercial (unported, v3.0) License (http://creativecommons.org/licenses/by-nc/3.0/). By accessing the work you hereby accept the Terms. Non-commercial uses of the work are permitted without any further permission from Dove Medical Press Limited, provided the work is properly attributed. For permission for commercial use of this work, please see paragraphs 4.2 and 5 of our Terms (https://www.dovepress.com/terms.php).

and become the first host of metastatic cells.[3] SLN mapping and biopsy are therefore standard procedures for guiding the therapeutic decisions of various malignant tumors in the clinic. Accurate identification of SLNs and differentiation from other second-echelon lymph nodes (LNs) are essential for pathological examination and selection of LNs for surgical removal. Currently, SLN mapping is performed in clinics by labeling SLNs with a blue dye (eg, patent blue or methylene blue),[4] gamma-ray detection with a radioisotope (eg, technetium 99m),[5] near-infrared (NIR) fluorescent imaging with indocyanine green,[6] or their combinations. However, the aforementioned monomodal conventional tracers have still not fit clinical criteria ideally. For example, the small blue dye and indocyanine green molecules might quickly migrate from SLNs to second-echelon LNs.[7] Some patients even suffer from severe anaphylactic reactions after the injection of the blue dye.[8] Indocyanine green also has the shortcomings of instability, easy diffusion, and fluorescence quenching.[9] Compared to the blue dye and indocyanine green, technetium-99m has a prolonged retention time in SLNs. Nevertheless, the radioactivity and limited half-life restrict its clinical applications.[10] Exploring new tracers for SLN imaging is thus highly demanded.

Nanomaterials have attracted much attention for SLN mapping.[11] Black carbon nanoparticles (NPs) have been approved as a lymphatic tracer by the Chinese Food and Drug Administration.[12] When carbon NPs are injected into the tissue nearby a tumor, they quickly migrate to SLNs, which are then stained with a black color.[13] In addition, titanium nitride (TiN) nanoshells,[14] single-walled carbon nanotubes,[15] gold-shelled iron oxide nanoclusters,[16] copper sulfide NPs,[17] semiconducting polymer NPs,[18] core@shell-structured Raman NPs,[7,19] and organic NPs[20] have also been reported to act as the tracers of SLNs. The size, shape, and surface chemistry are the important parameters that affect the lymphatic affinities of diverse nanomaterials.[21] The particle size is especially critical in determining the rate of diffusion through the interstitium, which then affects the draining and retention of NPs in LNs.[18] In general, NPs are transported to LNs by two different size-dependent mechanisms.[22] NPs with sizes of 5–100 nm are transported quickly through lymphatic vessels to LNs within several hours as the first pathway, while larger NPs (100–200 nm) are first up-taken by dendritic cells through phagocytosis and then transported to LNs as the second pathway.[23] Although NPs with sizes between 10 and 200 nm have been mostly exploited for lymphatic delivery,[24] such small particles have been found to bypass LNs quickly.[22] Carbon NPs have also been found to quickly migrate from SLNs to regional LNs owing to their small size (150 nm).[25] Recently, NPs with sizes larger than 200 nm have also been reported to enter LNs through the second pathway.[26] Compared with small particles, the retention of large nanoparticles in LNs is longer.[27]

SLN imaging facilitates further elimination of metastatic LNs. Currently, clinically used methods to eliminate metastatic LNs include surgical removal, chemotherapy, radiotherapy, and radiofrequency ablation.[28] However, lymphatic metastasis is imperceptible and is always difficult to be efficiently ablated by these conventional methods. Multimodal imaging-guided therapy was recently reported to hold great potential for precise theranostics of lymphatic metastasis.[17,29] Compared with monomodal imaging, multimodal imaging can integrate both ideal sensitivity and spatiotemporal resolution because of its intrinsic advantages of individual imaging modality.[29] Photothermal therapy (PTT) has also been adopted in multimodal imaging-guided treatments for the elimination of metastatic LNs, as it is minimally invasive.[17,29] The photothermal agent converts light into heat and thus increases the local temperature, which induces cell death if it is high enough.[30] The PTT of SLNs has shown to inhibit pulmonary metastasis and prolong animal survival.[15,16] In these works, the absorption of the photothermal agents lies primarily in the first NIR window (650–950 nm, NIR-I). Light in the second NIR window (1000–1350 nm, NIR-II) has a deeper tissue penetration than that in NIR-I.[31] However, to the best of our knowledge, PTT in NIR-II has rarely been applied for the elimination of metastatic LNs.

Plasmonic nanostructures such as gold nanostructures have unique tunable optical properties including light absorption and scattering. Gold nanostructures have been well accepted as photothermal agents. In addition, the light scattering property of gold nanostructures can also be utilized for dark-field imaging.[32,33] Compared with bright-field imaging, dark-field imaging offers higher contrast.[34] The application of dark-field imaging in SLN mapping has not been reported yet. Recently, TiN nanostructures are emerging as promising alternatives to gold nanostructures. TiN nanostructures offer several advantages in comparison with gold ones. First, they show superior plasmonic properties over both the visible and NIR regions.[35] Second, TiN has a higher melting point than gold, which provides better thermal stability under high-temperature conditions.[36,37] Third, TiN is cheaper than gold. Fourth, TiN nanospheres of the same size have a higher light absorption efficiency in the NIR-II window than gold nanospheres.[38] In addition, TiN also possesses high chemical

stability. These attributes position TiN nanostructures as a versatile material for photothermal therapy and high-contrast imaging techniques. So far, the application of TiN nanostructures in SLN mapping has not been demonstrated yet.

In this work, TiN nanobipyramids (NBPs) are synthesized and used as the tracer for SLNs. The synthesized TiN NBPs appear black and can be readily internalized into SLNs when they are locally injected. The size-dependent accumulation of the TiN NBPs is studied, with the larger TiN NBPs (274 nm) showing higher accumulation in SLNs. In addition, owing to the strong light scattering property of the TiN NBPs, dark-field imaging of SLNs is also enabled. Compared with carbon NPs, the TiN NBPs exhibit strong plasmonic absorption in NIR-II, facilitating the PTT ablation of metastatic LNs. The TiN NBP-based photothermal ablation of metastatic LNs combined with the surgical removal of primary tumors shows the remarkable inhibition of pulmonary metastasis. Taken together, our work demonstrates a new tracer for SLN mapping and also presents a new strategy relying on PTT in NIR-II to prevent lymphatic metastasis.

Materials and Methods

Preparation of the TiN NBPs

A hydrothermal method and post nitridation treatment were used together to prepare the TiN NBPs.[39] Briefly, TiO_2 NBPs were first prepared using a hydrothermal method. A tetramethylammonium hydroxide solution (30 mL, 25 wt% in water) was prepared and heated to 80 °C in a water bath. Ethylene glycol (30 mL) and titanium isopropoxide (1 mL) were then added dropwise. The above-mixed solution was stirred vigorously until a clear solution was obtained. The reaction mixture was subsequently transferred into a Teflon autoclave and kept at 230 °C for 24 h. TiO_2 NBPs were thus produced. They were centrifuged and washed with ethanol three times. The size of the TiO_2 NBPs was adjusted by varying the amount of added titanium isopropoxide. After the TiO_2 NBPs were heated in a muffle furnace with flowing ammonia gas at 800 °C for 5 h, TiN NBPs were obtained. The TiN NBPs were functionalized with poly(ethylene glycol) (PEG)-dopamine to improve their colloidal stability.

Characterization of the TiN NBPs

Scanning electron microscopy (SEM) imaging of the TiN NBPs was performed on a JEOL JSM7800F microscope operated at 20 kV. Transmission electron microscopy (TEM) imaging of the TiN NBPs was performed on an FEI Tecnai Spirit microscope at an operating voltage of 120 kV. The extinction spectrum of the TiN NBPs was measured on a Lambda 950 ultraviolet/visible/NIR spectrophotometer. The hydrodynamic size and polydispersity index (PDI) of the TiN NBPs were determined by a Malvern Zetasizer Nano ZS90 system.

Determination of Photothermal Conversion Efficiency

An aqueous solution of the TiN NBPs (2 mL, 286 μg mL^{-1}) was prepared in a 1 cm square cuvette, with the optical density of the solution at 1064 nm adjusted to 2.0. The solution was irradiated with a 1064 nm laser (Changchun New Industries Optoelectronics Tech. Co., China) at powers ranging from 0.2 to 0.8 W for 20 min. A thermocouple microprobe was used to record the temperature of the solution. The probe was utterly submerged in the solution without exposure to the laser light. The temperature cooling curve was measured after the laser was switched off. The photothermal conversion efficiency of the TiN NBPs was calculated according to a previously developed method.[40] As control, a carbon NP solution (2 mL, 100 μg mL^{-1}, Chongqing LUMMY Pharmaceutical Co., China) with the equal optical density of 2.0 at 1064 nm was irradiated with the same laser, and the photothermal conversion efficiency was also determined.

Cell Culture

Murine breast cancer 4T1 and macrophage RAW 264.7 cell lines were obtained from American Type Culture Collection (ATCC, Manassas, VA, USA) and cultured in Dulbecco's modified Eagle's medium (DMEM, Thermo Fisher Scientific) containing 10% fetal bovine serum (FBS), 100 μg mL^{-1} streptomycin, and 100 U mL^{-1} penicillin, in a humidified incubator with 5% CO_2 at 37 °C.

Cellular Uptake Assay

Three thousand 4T1 or RAW 264.7 cells were seeded into each well of a 96-well plate. After 24 h incubation, the culture medium was replaced with a fresh medium containing the TiN NBPs (50 or 100 μg mL^{-1}) of different sizes (131, 161, or 274 nm). After further incubation for 24 h, the cells were washed with phosphate-buffered saline (PBS) extensively to remove any particles adsorbed on the cell surface. Subsequently, the cells were observed and photographed under an Olympus IX71 fluorescence microscope (Melville, NY, USA).

Cell Viability Assay

Three thousand 4T1 or RAW 264.7 cells were seeded into each well of a 96-well plate. After 24 h incubation, the culture medium was replaced with a fresh medium containing the TiN NBPs (274 nm, 0–125 μg mL^{-1}). After further incubation for 48 h, 3-(4,5-dimethyl-2-thiazolyl)-2,5-diphenyl-2-H-tetrazolium bromide (MTT) assay and calcein acetoxymethyl ester (calcein-AM) staining were separately performed to study the cell viability.

For the MTT assay, the medium was discarded, and a fresh medium (100 μL) containing MTT (0.5 mg mL^{-1}) was added into each well. After incubation for 3 h, the medium was discarded, and the resultant formazan crystal was dissolved with dimethyl sulfoxide (150 μL). The absorbance of each well was measured by a SpectraMax Paradigm multimode microplate reader (Molecular Devices, Sunnyvale, CA, USA) at 540 nm. The cell viability for each sample relative to the control was calculated.

For calcein-AM staining, the medium in each well was replaced with a fresh serum-free medium containing calcein-AM (2 μM, Thermo Fisher Scientific). After 30 min incubation at 37 °C, the cells were washed with a fresh medium. The green fluorescence of the cells was observed under the fluorescence microscope.

PTT in vitro

Three thousand 4T1 cells were seeded into each well of a 96-well plate. After 24 h incubation, the culture medium was replaced with a fresh medium containing the TiN NBPs (274 nm, 100 μg mL^{-1}), followed by further incubation for 24 h. The cover on the plate was removed for the PTT assay, and the designated wells were exposed to 1064 nm laser irradiation for 5 min. The laser power densities were set to 0–0.76 W cm^{-2}. After further 24 h incubation, MTT assay and calcein-AM staining were performed separately to determine the cell viability.

Animal Experiments

Six-week-old female BALB/c mice were used in all animal studies. All animal experiments were approved by the Animal Care and Use Committee of Macau University of Science and Technology. Animal welfare and experiments complied with the Guide for the Care and Use of Laboratory Animals (8^{th} edition, National Institutes of Health, USA).

Biocompatibility Study

The mice were injected subcutaneously in the paws of the right hindfeet with PBS (50 μL) or the TiN NBP sample (274 nm, 50 mg kg^{-1}, 50 μL). After 48 h, the main organs (heart, liver, spleen, lung, and kidney) were harvested for histological examination. The tissue samples were fixed in 10% formalin, processed routinely into paraffin, sectioned at 8 μm thickness, and stained with hematoxylin and eosin (H&E).

In vivo SLN Mapping

The mice were subcutaneously injected with the TiN NBPs (50 μL, 100 μg mL^{-1}) of different sizes (131, 161, 274 nm) into the right hindfoot paws. The mice were sacrificed after 24 h and the popliteal LNs were dissected. The popliteal LNs were photographed and H&E staining was performed.

Dark-Field Imaging of SLNs

The mice were subcutaneously injected with PBS (50 μL), the carbon NPs (50 μL, 100 μg mL^{-1}), and the TiN NBPs (50 μL, 100 μg mL^{-1}) at the right hindfoot paws, respectively. After 24 h, the mice were sacrificed and the popliteal LNs

were collected. The paraffin slices (8 μm thickness) of the LNs were prepared for dark-field imaging. The samples were vacuum-dried and placed on a clean glass slide, and the scattering images of the samples were performed on an Olympus BX53M optical microscope.

In vivo Lymphatic Metastasis Model

The mice were subcutaneously injected with one million 4T1 cells suspended in PBS (50 μL) into the right hindfoot paws. Twelve days after injection, the popliteal LNs showed as hard spherical lumps indicating lymphatic metastasis.

PTT of SLNs in vivo

The 4T1-tumor bearing mice with popliteal LN metastasis were randomly divided into two groups (n = 5). PBS (50 μL) and the TiN NBPs (50 μL, 100 μg mL^{-1}) were injected into the tumors, respectively. After 24 h, all the mice were anesthetized through intraperitoneal injection of 1.5% pentobarbital sodium (75 mg kg^{-1}). Afterward, the SLNs of the mice were irradiated with the 1064 nm laser (0.76 W cm^{-2}, 5 min). The thermographic photos of the mice and the temperature changes of the SLNs were acquired using a FLIR ONE Pro thermal camera (FLIR Systems, Portland, OR, USA) during laser irradiation.

Effect of SLN PTT on Pulmonary Metastasis

The 4T1-tumor bearing mice with popliteal LN metastasis were randomly divided into four groups (n = 5). The mice were treated as follows: (1) control, with PBS (50 μL) injected into the tumors only; (2) surgery only, where surgical removal of the primary tumors of the mice was performed without injection of the TiN NBPs; (3) surgery plus the TiN NBPs, where surgical removal of the primary tumors was performed 24 h after the injection of the TiN NBPs (50 μL, 100 μg mL^{-1}); (4) PTT of SLNs with the TiN NBPs together with the assistance of surgery. The TiN NBPs (50 μL, 100 μg mL^{-1}) were injected into the tumors, and the primary tumors of the mice were removed by surgery after 24 h. The SLNs were irradiated with the 1064 nm laser (0.76 W cm^{-2}, 5 min) simultaneously. The weights of the mice were monitored every other day post various treatments.

Pulmonary Metastasis Assay

The mice were sacrificed on day 22 after the treatments. India ink (15%) was perfused into the lungs through the trachea, and the lungs were soaked in a Fekete's solution (70% ethanol, 3.7% formaldehyde, 0.75 M glacial acetic acid) for 48 h at room temperature. The lungs were photographed, and the numbers of the tumor nodules (shown as white spots on the surface of the lungs) were counted.

Statistical Analysis

The results are expressed as means ± standard errors of the means (S.E.M.) based on at least three independent experiments. The statistical differences were evaluated with a one-way analysis of variance (ANOVA) followed by Tukey's post hoc test. A $P < 0.05$ was considered statistically significant.

Results and Discussion

Synthesis and Characterization of the TiN NBPs

TiN nanostructures are low-cost, thermally and chemically stable They are usually prepared through various plasma techniques.[39] However, the obtained TiN nanostructures are often attached to substrates, which hampers their further biological applications. In this study, the TiN NBPs were prepared by a combination of a hydrothermal method and post nitridation treatment.[41] TiO_2 NBPs were first prepared using a hydrothermal method. The size can be easily adjusted by changing the ratio of the reactants. They were then subjected to nitridation treatment in a muffle furnace with flowing ammonia gas at 800 °C for 5 h. The SEM and TEM images of the obtained TiN NBPs are displayed in Figure 1a. The prepared TiN NBPs show great uniformity in shape and size. The TiN NBPs have an arc-shaped base at the waist and two blunt apexes. Three TiN-NBP samples with different sizes were synthesized. Their lengths are 131 ± 14, 161 ± 7, and

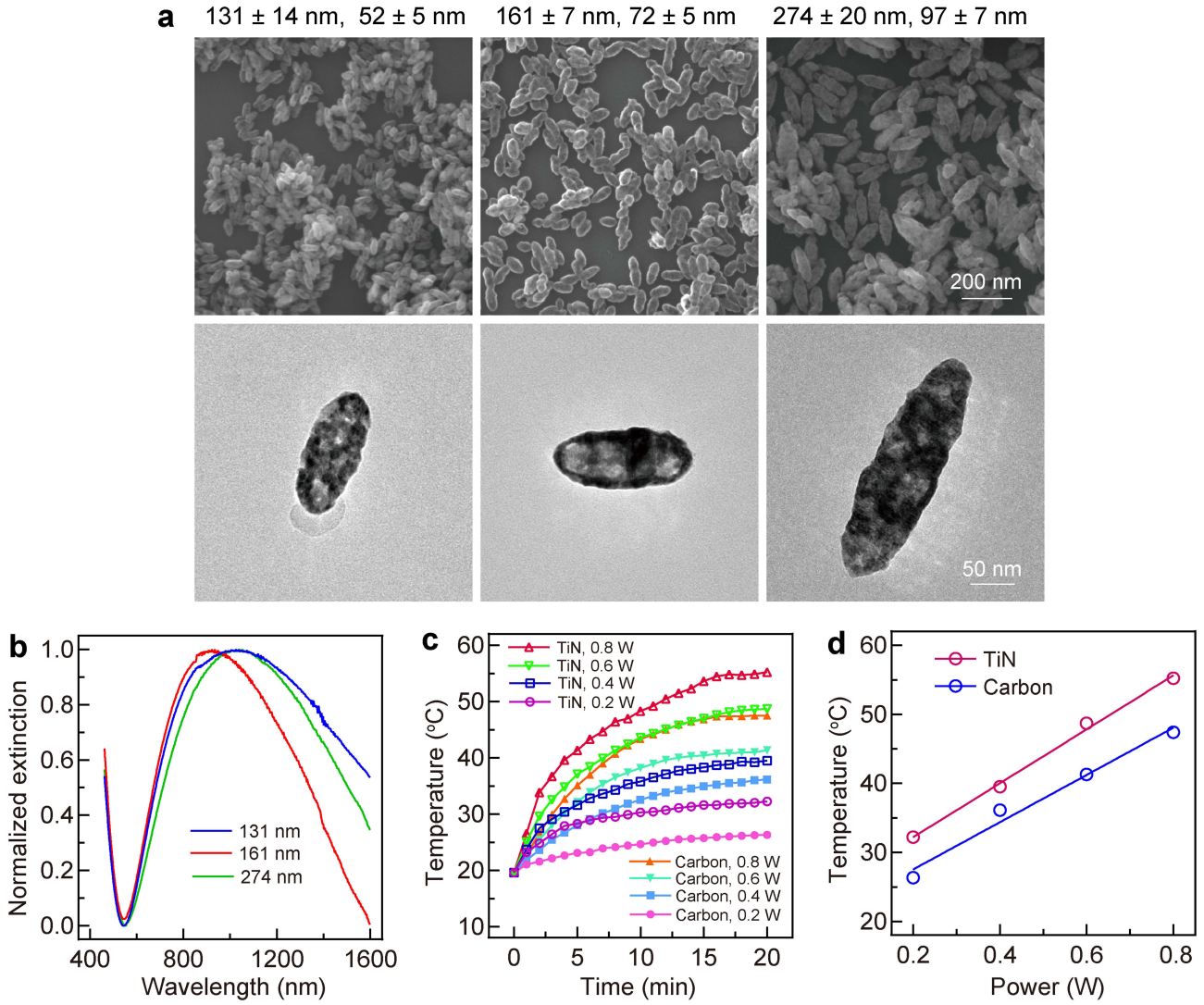

Figure 1 Characterization of the TiN NBPs. (**a**) SEM (upper row) and TEM (lower row) images of the TiN NBPs. (**b**) Extinction spectra of the TiN NBPs in aqueous solutions. (**c**) Temperature rise curves of the carbon NPs (2 mL, extinction value at 1064 nm E_{1064} = 2, 100 μg mL^{-1}) and 274 nm TiN NBPs (2 mL, E_{1064} = 2, 286 μg mL^{-1}) acquired under 1064 nm laser irradiation at different optical powers for 20 min. (**d**) Variation of the reached plateau temperature with the laser power. The data are extracted from (**c**).

274 ± 20 nm, with their waist widths being 52 ± 5, 72 ± 5, and 97 ± 7nm, respectively. Their hydrodynamic particle sizes measured by dynamic light scattering analysis are 154 ± 0.2, 237 ± 0.4, 295 ± 0.3 nm, respectively (Figure S1).

Compared to the NIR-I window, light in the NIR-II window has much deeper tissue penetration because of less absorption and scattering of light by tissues and blood.[42] Light with wavelengths in the range of 1000–1100 nm is believed to have maximal penetration depth. Common photothermal agents such as Au nanorods[43] and CuS NPs[17] are only responsive in the NIR-I window so far. The localized surface plasmon resonance (LSPR) of TiN nanostructures is easily tunable in the optically transparent window in biology,[44] which is essential for PTT applications.[45] The extinction spectra of the three TiN-NBP samples are shown in Figure 1b, and their longitudinal plasmon resonance peaks are 1036, 922, and 1040 nm, respectively. Therefore, the synthesized TiN NBPs can be used as a PTT agent responsive in the NIR-II window.[45] In addition, TiN has a rather high melting point (2930 °C), and the TiN NBPs are believed to have high photothermal stability.

Photothermal Conversion Efficiency of the TiN NBPs

The photothermal conversion efficiency of the TiN NBPs was determined under 1064 nm laser irradiation and compared with the carbon NPs, which do not have any absorption peak in the NIR-II region (Figure S2). Figure 1c displays the

temperature rise curves of the aqueous carbon NP and TiN NBP solutions under 1064 nm laser irradiation at optical powers ranging from 0.2 to 0.8 W. The temperature of the solution quickly increases in 15 min and reaches a plateau at 20 min of irradiation. The temperature reached at the plateau increases with the increment of the laser power. The end temperature of the TiN NBP solution reaches 32.2, 39.5, 48.7, and 55.2 °C at the optical power of 0.2, 0.4, 0.6, and 0.8 W, respectively. In comparison, the end temperature of the carbon NP solution reaches 26.3, 36.1, 41.3, and 47.4 °C, respectively (Figure 1d). A reported theoretical model[40] was employed to calculate the photothermal conversion efficiency (η) according to the equation below

$$\eta = \frac{hS(T_{end} - T_0) - Q_{diss}}{I\left(1 - 10^{-E_{1064}}\right)} \quad (1)$$

where h is the heat transfer coefficient, and S is the heat-transfer surface area. The hS value was obtained from Figures 1c and S3. T_0 and T_{end} are the temperatures of the carbon NP and TiN NBP solution before and after laser irradiation, respectively. I is the laser power, and E_{1064} is the extinction value of the carbon NP or TiN NBP solution at 1064 nm. Q_{diss} is the heat dissipated from light absorbed by the solvent and the container. According to the equation above, the photothermal conversion efficiency of the TiN NBPs and carbon NPs were determined to be (93.7 ± 0.4)% and (80.4 ± 1.7)% under 1064 nm laser irradiation, respectively.

Cytotoxicity and Cellular Uptake of the TiN NBPs

The cytotoxicity and cellular uptake of the TiN NBPs were studied in murine mammary carcinoma 4T1 and macrophage RAW 264.7 cells. The cell viability was determined by MTT assay. The TiN NBPs show no clear cytotoxicity in both 4T1 (Figure 2a) and RAW 264.7 cells (Figure S4a). The viability of the cells after the treatment with the TiN NBPs (125 μg mL^{-1}) remains ~80%. These results indicate that the TiN NBPs have good biocompatibility.

The biomedical applications of nanomaterials are largely dependent on their intracellular distribution. The nanoparticle size is one of the key factors affecting their cellular uptake.[46] The effect of the size on the cellular uptake for the TiN NBPs was thus evaluated. Among the three samples, the largest TiN NBPs (274 nm) display a higher cellular uptake efficiency in both 4T1 (Figure 2b) and RAW 264.7 cells (Figure S4b). The TiN NBPs with the size of 274 nm were therefore further used in our experiments.

PTT in vitro

In recent years, PTT agents responsive in NIR-II have attracted much attention in cancer therapy. However, the low light-to-heat conversion efficiency is still a barrier for these PTT agents for further applications. The high photothermal conversion efficiency of the TiN NBPs shown above motivated us to carry out in vitro PTT studies with the TiN NBPs. For 4T1 cells, 1064 nm laser irradiation in the absence of the TiN NBPs did not affect the viability of the cells. However, the laser irradiation on the cells in the presence of the TiN NBPs (274 nm, 100 μg mL^{-1}) resulted in remarkable cytotoxicity, which was dependent on the laser power density. The survival rates of the cells declined to (90.6 ± 1.9)%, (64.8 ± 7.9)%, (39.1 ± 8.9)%, and (14.1 ± 0.4)% when the laser power densities were 0.24, 0.51, 0.64, and 0.76 W cm^{-2}, respectively (Figure 2c). Calcein-AM staining (Figure 2d) further confirmed this result. The live cells were stained with green fluorescence. When the cells were subjected to laser irradiation at a power density of 0.51 and 0.64 W cm^{-2}, most cells were observed to become round or dead. Nearly all the cells were ablated after the laser irradiation at 0.76 W cm^{-2} for 5 min.

TiN NBPs for SLN Mapping

The size of nanoparticles is one of the critical parameters determining the diffusion rate through the interstitium, draining in the lymphatic system, and uptake by LNs.[26] Small NPs are usually accepted to be drained more in LNs, while larger particles prolong the retention in LNs.[27] The long retention of the SLN tracer is believed to provide a suitable surgical time window to meet clinical needs.

In the in vivo study, the TiN NBPs coated with PEG were used. After PEG coating, the PDI of 274 nm TiN NBPs decreases to 0.25 (below 0.3) from 0.36, indicating PEG coating significantly improves their dispersity and PEG-coated

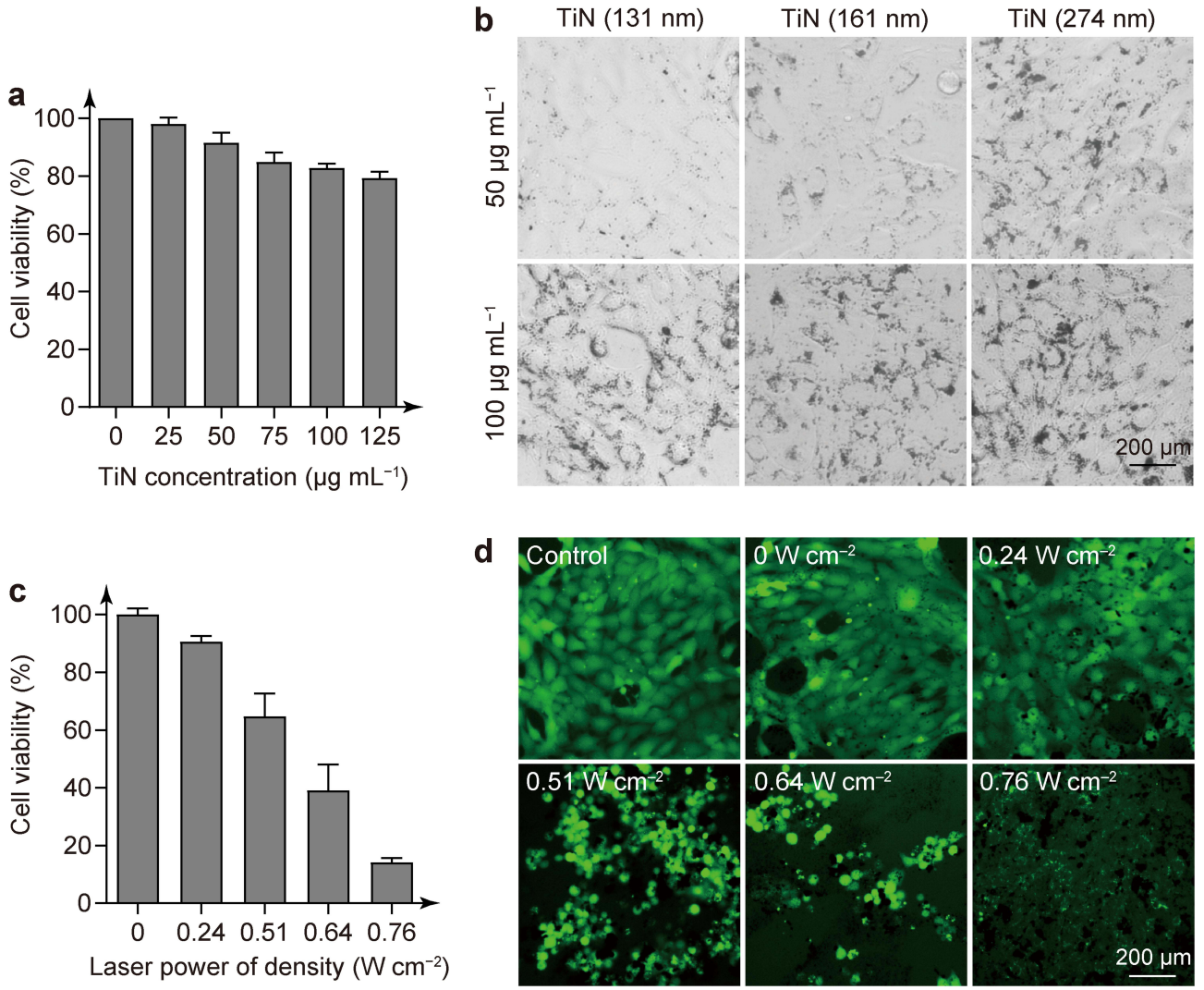

Figure 2 Cytotoxicity, cellular uptake, and PTT in 4T1 cells. (**a**) Effect of the 274 nm TiN NBPs at different concentrations on the viability of 4T1 cells. The 4T1 cells were treated with 274 nm TiN NBPs (0–125 μg mL^{-1}) for 48 h, MTT assay was performed to determine the cell viability. (**b**) Cellular uptake of the TiN NBPs in 4T1 cells. The 4T1 cells were treated with TiN NBPs with different sizes (131, 161, and 274 nm) and concentrations (50 and 100 μg mL^{-1}) for 24 h, the intracellular distribution of TiN NBPs was observed under a microscope. (**c**) Cell viabilities of 4T1 cells upon PTT at different optical power densities. (**d**) Calcein-AM staining of the cells treated by PTT at different optical power densities as in (**c**). The 4T1 cells were treated with 274 nm TiN NBPs (100 μg mL^{-1}) for 24 h, followed by exposure to 1064 nm laser irradiation at different optical power densities (0–0.76 W cm^{-2}). After 24 h incubation, MTT assay and calcein-AM staining were performed separately to determine the cell viability and live cells. The data shown represent the mean ± S.E.M. $n = 3$.

TiN NBPs are monodisperse. For SLN mapping, we found that the TiN NBPs readily drained into the SLNs when they were locally injected around the primary tumor.[14] The SLNs were stained with black color. This phenomenon is similar to that of the carbon NPs used clinically. The effect of the size of the TiN NBPs on LN tracing was examined first. Mice were subcutaneously injected into the right hindfoot paws with the TiN NBPs (50 μL, 100 μg mL^{-1}) of different sizes. The mice were sacrificed after 24 h, and their popliteal LNs were dissected. As shown in Figure 3a, the popliteal LNs were stained with black color by the TiN NBPs. Further H&E staining of the section slices indicated that most TiN NBPs were accumulated at the subcapsular sinus (Figure 3b) where cancer cells initially accumulated during lymphatic metastasis.[47] Among the three samples, the largest TiN NBPs with the size of 274 nm showed the most accumulation in the LNs (Figure 3a and b), and some particles even diffused toward the cortex of the LNs (Figure 3b).

We also harvested the major organs (heart, liver, spleen, lung, and kidney) from the mice and performed H&E staining on the section slices to study the biocompatibility of the TiN NBPs. As shown in Figure S5, there is no

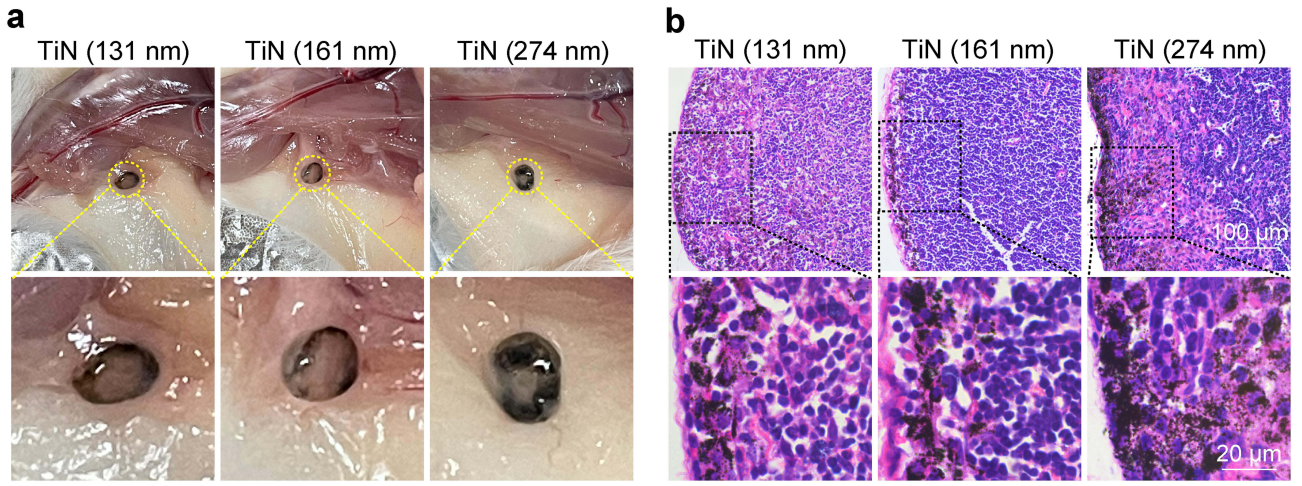

Figure 3 Size-dependent SLN mapping with TiN NBPs. (**a**) TiN NBPs (50 mg kg^{-1}) with lengths of 131 nm, 161 nm, and 274 nm were injected into the hindfoot paws of the mice. The mice were then sacrificed 24 h later, and the popliteal LNs were dissected and photographed. (**b**) H&E staining of the section slices of the LNs from the mice treated with the different lengths of TiN NBPs for 24 h. The black TiN NBPs are mainly distributed in the subcapsular sinus of the LNs.

noticeable organ damage or inflammation after the treatment of the TiN NBPs. These results indicate that the biocompatible TiN NBPs with large sizes are a good candidate tracer for SLN mapping.

TiN NBPs for the Dark-Field Imaging of SLNs

The LSPR of plasmonic nanoparticles enables them as nanoprobes for imaging. Their large scattering cross-sections can give high signal-to-background ratios for dark-field imaging.[48] The image contrast under dark-field microscopy (DFM) comes from the elastic scattering of light by plasmonic NPs, which generates bright dots on dark-field scattering images. More importantly, the scattering spectrum is very sensitive to the morphology of nanostructures themselves.[49] The NBP structures exhibit highly polarization-dependent absorption and scattering cross-sections because of their anisotropic geometry.[50] They are a potential contrast agent for dark-field imaging. The TiN NBPs were therefore further explored for the dark-field imaging of SLNs.

After tracing with either the TiN NBPs or carbon NPs, the popliteal LNs were stained with black color. The two types of tracers showed a similar performance under bright-field imaging (Figure 4a). However, compared with the carbon-NP-stained LNs, the LNs stained with the TiN NBPs showed a substantial scattering signal under DFM (Figure 4a). This result was further confirmed by the observation of the section slices of the LNs under DFM (Figure 4b). A large number of bright dots were observed in the slices of the LNs stained with the TiN NBPs under DFM. These results indicate that apart from tracing SLNs with black color, the label-free TiN NBPs can also be used as a contrast agent for the dark-field imaging of SLNs.

PTT of SLNs in vivo

Removal of LNs invaded by metastatic cells is essential to prevent the spread of cancer cells post-surgery. Several previous studies have suggested that the PTT ablation of SLNs is able to prevent tumor metastasis.[15,16] However, the LSPR peaks of the photothermal agents used in the previous works lie primarily in the NIR-I region. Compared with NIR-I light, light in NIR-II exhibits deeper tissue penetration and higher maximal permissible exposure.[51] The TiN NBPs responsive in NIR-II were therefore used for the PTT ablation of SLNs for the prevention of cancer metastasis in a lymphatic metastasis model.

The 4T1 cells were subcutaneously injected into the paws of the right hindfeet of the mice. Owing to the enriched lymphatic vessels in the paws, the tumor cells migrated to the near SLNs in 12 days. The popliteal LNs became swollen owing to invasion by the metastatic cancer cells. The photothermal ablation of the SLNs was then performed and it was combined with the surgical removal of the primary tumors to prevent lymphatic metastasis (Figure 5a).

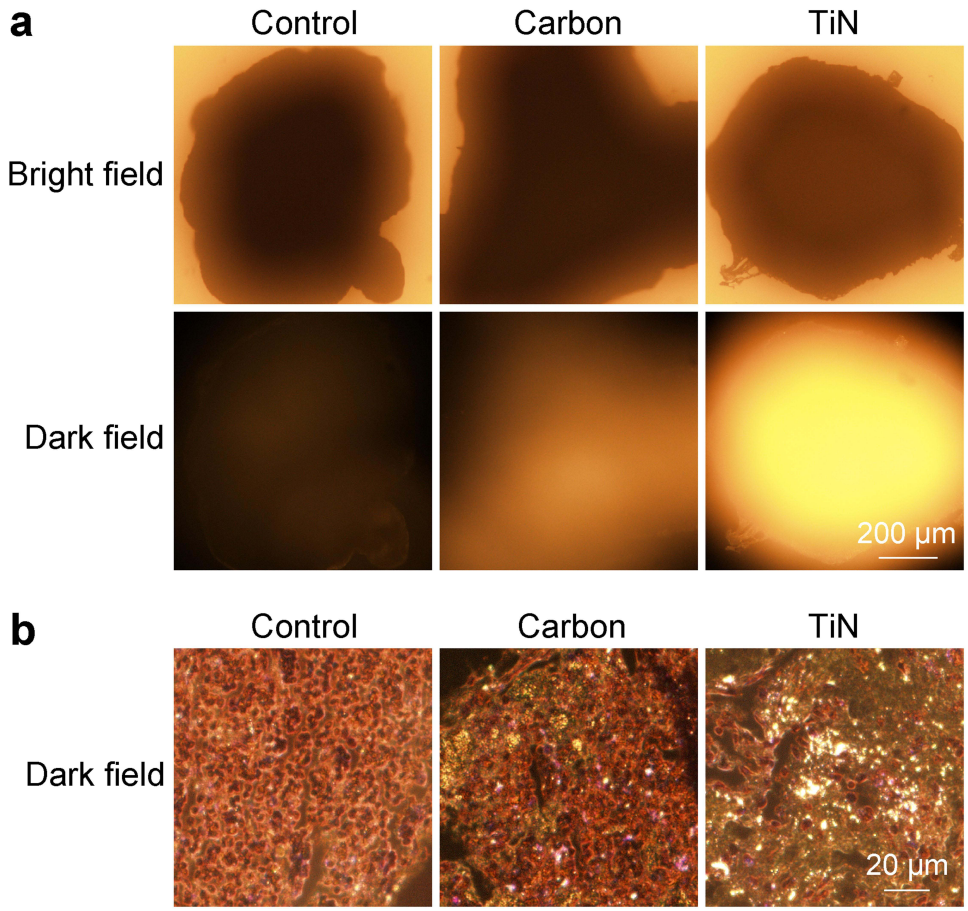

Figure 4 Dark-field imaging of SLNs with the TiN NBPs. (**a**) Bright-field and dark-field imaging of SLNs with the carbon NPs or TiN NBPs ex vivo. (**b**) Dark-field imaging of the section slices of SLNs. Twenty-four hours after the carbon NPs or TiN NBPs (50 mg kg^{-1}) were injected to the hindfoot paws of the mice, the mice were sacrificed and the popliteal LNs were dissected and photographed under both the bright- and dark-field modes. The section slices were also observed under DFM.

The laser irradiation of the SLNs at the power density of 0.76 W cm^{-2} for 5 min induced a negligible temperature increase in the control group, while the irradiation at this power density induced a steady increase in temperature. After 5 min irradiation, the temperature of the SLNs reached as high as 56.8 ± 1.2 °C (Figure 5b and c). Such a high temperature is enough to completely ablate the metastatic cancer cells in the SLNs. All mice were sacrificed 22 days after the treatments, and the popliteal LNs were resected. As shown in Figure 5d and e, PTT significantly reduced the size and weight of the LNs.

Inhibition of Pulmonary Metastasis Through the PTT Ablation of SLNs

Lung is one of the target organs for cancer metastasis. The resultant pulmonary metastasis is the common reason for the death of cancer patients. The effect of a combination of PTT ablation of SLNs and surgical resection of primary tumors on pulmonary metastasis was compared with that of the single treatment. There is no death or significant weight loss for the mice from each group (Figure S6). All the mice were sacrificed at the end of the treatment, and the lungs were stained with India ink. The metastatic nodules in the lung showed as white spots (Figure 6a). There were a number of metastatic nodules in the lungs of the untreated mice, and the weight of the lungs from this group was even the largest among the four groups (Figure 6b). Surgical resection of the primary tumors was not enough to prevent pulmonary metastasis, as a number of the nodules were still observed in the lungs. However, the combined treatment of SLN-ablation with PTT and surgery significantly reduced the number of metastatic nodules (Figure 6a and c). H&E staining of the section slices of the LNs further confirmed this result (Figure 6d).

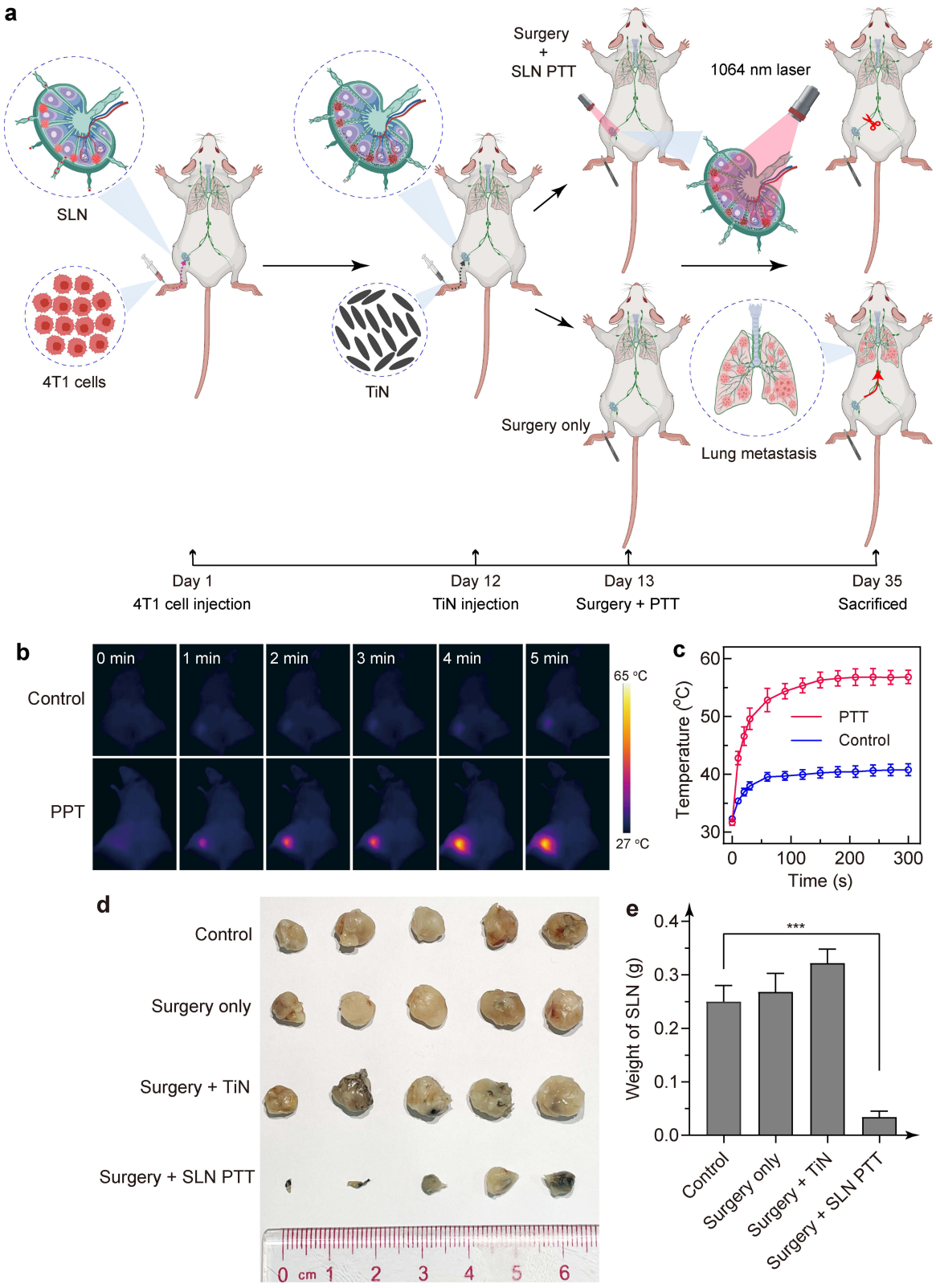

Figure 5 PTT of SLNs in vivo. (**a**) Schematic illustrating the design of the experiment. 4T1 cells were inoculated subcutaneously into the right hindfoot paws of the mice. The tumor cells spread into the SLN around the inner knee of the mice in 12 days. The TiN NBPs were intratumorally injected. They migrated into the SLNs through lymphatic vessels. PTT was then performed by exposing the LNs to the 1064 nm laser. Pulmonary metastasis happened in the mice with resection of primary tumors only. However, significant less metastatic nodules were observed in the lungs from those with combined surgery and SLN-ablation with PTT. (**b**) Infra-red thermal images of the LNs subjected to 1064 nm laser irradiation at 0.76 W cm^{-2} for 5 min. (**c**) Temperature change curves of the SLNs extracted from (**b**). (**d**) Images of the SLNs after various treatments. The mice were sacrificed 22 days after the treatments and the popliteal LNs were dissected. (**e**) Weight of the SLNs after each treatment. The data shown represent the mean ± S.E.M. $n = 5$, $^{***}P < 0.001$.

https://doi.org/10.2147/IJN.S488480 DovePress

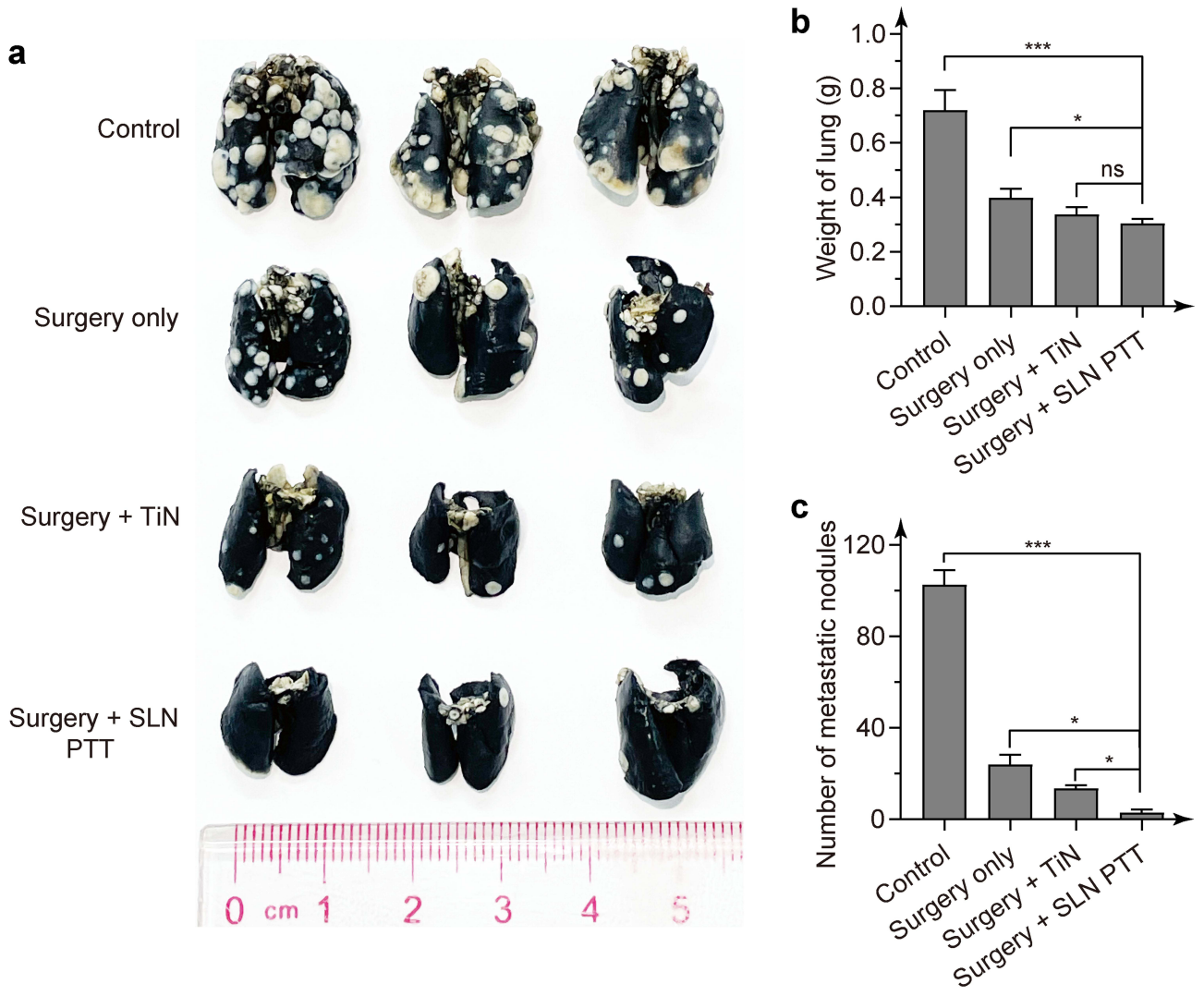

Figure 6 Inhibition of pulmonary metastasis through the PTT ablation of SLNs. (**a**) Photographs of the entire lungs stained with India ink. The mice were sacrificed at 22 days after various treatments, and the entire lungs were dissected after the intratracheal injection of Indian ink. The white nodules represent lung metastasis. (**b**) The number of metastatic nodules in the lungs estimated from (**a**). (**c**) Weight of the lungs for each treatment. (**d**) H&E staining of the lung slices. The metastatic nodules in the lungs were indicated with black circles. The data shown represent the mean ± S.E.M. $n = 3$, $^{***}P < 0.001$, $^{*}P < 0.05$.

Conclusions

In summary, TiN NBPs as a new type of tracer of SLNs have been demonstrated for SLN mapping. The accumulation of the TiN NBPs in the SLNs is dependent on their size. The TiN NBPs with a size of 274 nm show the best drainage in SLNs. The TiN NBPs enable both black staining and dark-field imaging of SLNs. Furthermore, the TiN NBP-based

photothermal ablation of metastatic SLNs combined with surgical removal of primary tumors demonstrate remarkable inhibition of pulmonary metastasis. This multifunctional platform offers great potential for both multimodal mapping and therapy of lymph node metastasis in the future.

Acknowledgments

Y.-N. Xu, X.P. Bai, and J.-L. Chen contributed equally to this work. This work was supported by the Science and Technology Development Fund, Macau SAR (File no. 0035/2022/A1 and 006/2023/SKL) and the Guangdong Basic and Applied Basic Research Foundation (General Research Fund, 2022A1515010247).

Disclosure

The authors declare no conflict of interest.

References

1. Ganesh K, Massagué J. Targeting metastatic cancer. *Nat Med*. 2021;27(1):34–44. doi:10.1038/s41591-020-01195-4
2. Karaman S, Detmar M. Mechanisms of lymphatic metastasis. *J Clin Invest*. 2014;124(3):922–928. doi:10.1172/JCI71606
3. Leong SP, Pissas A, Scarato M, et al. The lymphatic system and sentinel lymph nodes: conduit for cancer metastasis. *Clin Exp Metastasis*. 2022;39(1):139–157. doi:10.1007/s10585-021-10123-w
4. Ang CH, Tan MY, Teo C, et al. Blue dye is sufficient for sentinel lymph node biopsy in breast cancer. *Br J Surg*. 2014;101(4):383–389. doi:10.1002/bjs.9390
5. Ahmed M, Purushotham AD, Horgan K, et al. Meta-analysis of superficial *versus* deep injection of radioactive tracer and blue dye for lymphatic mapping and detection of sentinel lymph nodes in breast cancer. *Br J Surg*. 2015;102(3):169–181. doi:10.1002/bjs.9673
6. Cousins A, Thompson SK, Wedding AB, et al. Clinical relevance of novel imaging technologies for sentinel lymph node identification and staging. *Biotechnol Adv*. 2014;32(2):269–279. doi:10.1016/j.biotechadv.2013.10.011
7. Deng BG, Wang YH, Wu YF, et al. Raman nanotags-guided intraoperative sentinel lymph nodes precise location with minimal invasion. *Adv Sci*. 2022;9(2):e2102405. doi:10.1002/advs.202102405
8. Barthelmes L, Goyal A, Sudheer P, et al. Investigation of anaphylactic reaction after patent blue V dye injection. *Breast*. 2010;19(6):516–520. doi:10.1016/j.breast.2010.05.016
9. Porcu EP, Salis A, Gavini E, et al. Indocyanine green delivery systems for tumour detection and treatments. *Biotechnol Adv*. 2016;34(5):768–789. doi:10.1016/j.biotechadv.2016.04.001
10. Ahmed M, Purushotham AD, Douek M. Novel techniques for sentinel lymph node biopsy in breast cancer: a systematic review. *Lancet Oncol*. 2014;15(8):e351–362. doi:10.1016/S1470-2045(13)70590-4
11. Han M, Kang RR, Zhang CQ. Lymph node mapping for tumor micrometastasis. *ACS Biomater Sci Eng*. 2022;8(6):2307–2320. doi:10.1021/acsbiomaterials.2c00111
12. Liu PC, Tan J, Tan QW, et al. Application of carbon nanoparticles in tracing lymph nodes and locating tumors in colorectal cancer: a concise review. *Int J Nanomed*. 2020;15:9671–9681. doi:10.2147/IJN.S281914
13. Tian Y, Yang PG, Lin YC, et al. Assessment of carbon nanoparticle suspension lymphography-guided distal gastrectomy for gastric cancer. *JAMA Network Open*. 2022;5(4):e227739. doi:10.1001/jamanetworkopen.2022.7739
14. Wu X, Wang L, Xu Y-N, et al. Chemo-phototherapy with carfilzomib-encapsulated TiN nanoshells suppressing tumor growth and lymphatic metastasis. *Small*. 2022;18(29):2200522. doi:10.1002/smll.202200522
15. Liang C, Diao S, Wang C, et al. Tumor metastasis inhibition by imaging-guided photothermal therapy with single-walled carbon nanotubes. *Adv Mater*. 2014;26(32):5646–5652. doi:10.1002/adma.201401825
16. Liang C, Song XJ, Chen Q, et al. Magnetic field-enhanced photothermal ablation of tumor sentinel lymph nodes to inhibit cancer metastasis. *Small*. 2015;11(37):4856–4863. doi:10.1002/smll.201501197
17. Shi H, Yan RQ, Wu LY, et al. Tumor-targeting CuS nanoparticles for multimodal imaging and guided photothermal therapy of lymph node metastasis. *Acta Biomater*. 2018;72:256–265. doi:10.1016/j.actbio.2018.03.035
18. Yang Z, Tian R, Wu JJ, et al. Impact of semiconducting perylene diimide nanoparticle size on lymph node mapping and cancer imaging. *ACS Nano*. 2017;11(4):4247–4255. doi:10.1021/acsnano.7b01261
19. Bao ZZ, Zhang YQ, Tan ZY, et al. Gap-enhanced Raman tags for high-contrast sentinel lymph node imaging. *Biomaterials*. 2018;163:105–115. doi:10.1016/j.biomaterials.2018.02.020
20. Fan XX, Li YR, Feng Z, et al. Nanoprobes-assisted multichannel NIR-II fluorescence imaging-guided resection and photothermal ablation of lymph nodes. *Adv Sci*. 2021;8(9):2003972. doi:10.1002/advs.202003972
21. Ke XY, Howard GP, Tang HY, et al. Physical and chemical profiles of nanoparticles for lymphatic targeting. *Adv Drug Deliv Rev*. 2019;151−152:72–93. doi:10.1016/j.addr.2019.09.005
22. Luo M, Samandi LZ, Wang ZH, et al. Synthetic nanovaccines for immunotherapy. *J Control Release*. 2017;263:200–210. doi:10.1016/j.jconrel.2017.03.033
23. Najibi AJ, Mooney DJ. Cell and tissue engineering in lymph nodes for cancer immunotherapy. *Adv Drug Deliv Rev*. 2020;161−162:42–62. doi:10.1016/j.addr.2020.07.023
24. Chen Y, De Koker S, De Geest BG. Engineering strategies for lymph node targeted immune activation. *Acc Chem Res*. 2020;53(10):2055–2067. doi:10.1021/acs.accounts.0c00260
25. Chen ZY, Zhong ZM, Chen GQ, et al. Application of carbon nanoparticles in neck dissection of clinically node-negative papillary thyroid carcinoma. *Biomed Res Int*. 2021;2021:6693585. doi:10.1155/2021/6693585

26. Lin ZB, Xi L, Chen SK, et al. Uptake and trafficking of different sized PLGA nanoparticles by dendritic cells in imiquimod-induced psoriasis-like mice model. *Acta Pharm Sin B*. 2021;11(4):1047–1055. doi:10.1016/j.apsb.2020.11.008
27. Zhang Y-N, Lazarovits J, Poon W, et al. Nanoparticle size influences antigen retention and presentation in lymph node follicles for humoral immunity. *Nano Lett*. 2019;19(10):7226–7235. doi:10.1021/acs.nanolett.9b02834
28. Pan T, Xie Q-K, Lv N, et al. Percutaneous CT-guided radiofrequency ablation for lymph node oligometastases from hepatocellular carcinoma: a propensity score-matching analysis. *Radiology*. 2017;282(1):259–270. doi:10.1148/radiol.2016151807
29. Cai W, Fan GH, Zhou H, et al. Self-assembled hybrid nanocomposites for multimodal imaging-guided photothermal therapy of lymph node metastasis. *ACS Appl Mater Interfaces*. 2020;12(4):49407–49415. doi:10.1021/acsami.0c14576
30. Liu YJ, Bhattarai P, Dai ZF, et al. Photothermal therapy and photoacoustic imaging via nanotheranostics in fighting cancer. *Chem Soc Rev*. 2019;48(7):2053–2108. doi:10.1039/c8cs00618k
31. Chen J-L, Zhang H, Huang X-Q, et al. Antiangiogenesis-combined photothermal therapy in the second near-infrared window at laser powers below the skin tolerance threshold. *Nano-Micro Lett*. 2019;11(1):93. doi:10.1007/s40820-019-0327-4
32. Sobral-Filho RG, DeVorkin L, Macpherson S, et al. Ex vivo detection of circulating tumor cells from whole blood by direct nanoparticle visualization. *ACS Nano*. 2018;12(2):1902–1909. doi:10.1021/acsnano.7b08813
33. Zhang Q, Yan HH, Ru C, et al. Plasmonic biosensor for the highly sensitive detection of microRNA-21 via the chemical etching of gold nanorods under a dark-field microscope. *Biosens Bioelectron*. 2022;201:113942. doi:10.1016/j.bios.2021.113942
34. Boamfa MI, Asselman MJA, Vulders RCM, et al. Combined transmission, dark field and fluorescence microscopy for intact, 3D tissue analysis of biopsies. *J Biomed Opt*. 2020;25(11):116503. doi:10.1117/1.JBO.25.11.116503
35. Wang CM, Dai C, Hu ZQ, et al. Photonic cancer nanomedicine using the near infrared-II biowindow enabled by biocompatible titanium nitride nanoplatforms. *Nanoscale Horiz*. 2019;4(2):415–425. doi:10.1039/c8nh00299a
36. Naik GV, Shalaev VM, Boltasseva A. Alternative plasmonic materials: beyond gold and silver. *Adv Mater*. 2013;25(24):3264–3294. doi:10.1002/adma.201205076
37. Reddy H, Guler U, Kudyshev Z, et al. Temperature-dependent optical properties of plasmonic titanium nitride thin films. *ACS Photonics*. 2017;4(6):1413–1420. doi:10.1021/acsphotonics.7b00127
38. Ishii S, Sugavaneshwar RP, Nagao T. Titanium nitride nanoparticles as plasmonic solar heat transducers. *J Phys Chem C*. 2016;120(4):2343–2348. doi:10.1021/acs.jpcc.5b09604
39. Bai XP, Lam SH, Hu JT, et al. Colloidal plasmonic TiN nanoparticles for efficient solar seawater desalination. *ACS Appl Mater Interfaces*. 2023;15(48):55856–55869. doi:10.1021/acsami.3c13479
40. Liu XJ, Li B, Fu FF, et al. Facile synthesis of biocompatible cysteine-coated CuS nanoparticles with high photothermal conversion efficiency for cancer therapy. *Dalton Trans*. 2014;43(30):11709–11715. doi:10.1039/c4dt00424h
41. Yick S, Murdock AT, Martin PJ, et al. Tuning the plasmonic response of TiN nanoparticles synthesised by the transferred arc plasma technique. *Nanoscale*. 2018;10(16):7566–7574. doi:10.1039/c7nr09309h
42. Smith AM, Mancini MC, Nie SM. Bioimaging: second window for in vivo imaging. *Nat Nanotechnol*. 2009;4(11):710–711. doi:10.1038/nnano.2009.326
43. Zhu X-M, Fang CH, Jia HL, et al. Cellular uptake behaviour, photothermal therapy performance, and cytotoxicity of gold nanorods with various coatings. *Nanoscale*. 2014;6(19):11462–11472. doi:10.1039/c4nr03865g
44. Naik GV, Kim J, Boltasseva A. Oxides and nitrides as alternative plasmonic materials in the optical range. *Opt Mater Express*. 2011;1(6):1090–1099. doi:10.1364/OME.1.001090
45. Xu C, Pu KY. Second near-infrared photothermal materials for combinational nanotheranostics. *Chem Soc Rev*. 2021;50(2):1111–1137. doi:10.1039/d0cs00664e
46. Canton I, Battaglia G. Endocytosis at the nanoscale. *Chem Soc Rev*. 2012;41(7):2718–2739. doi:10.1039/c2cs15309b
47. Jalkanen S, Salmi M. Lymphatic endothelial cells of the lymph node. *Nat Rev Immunol*. 2020;20(9):566–578. doi:10.1038/s41577-020-0281-x
48. Anker JN, Hall WP, Lyandres O, et al. Biosensing with plasmonic nanosensors. *Nat Mater*. 2008;7(6):442–453. doi:10.1038/nmat2162
49. Wang W. Imaging the chemical activity of single nanoparticles with optical microscopy. *Chem Soc Rev*. 2018;47(7):2485–2508. doi:10.1039/c7cs00451f
50. Chow TH, Li NN, Bai XP, et al. Gold nanobipyramids: an emerging and versatile type of plasmonic nanoparticles. *Acc Chem Res*. 2019;52(8):2136–2146. doi:10.1021/acs.accounts.9b00230
51. Ding XG, Liow CH, Zhang MX, et al. Surface plasmon resonance enhanced light absorption and photothermal therapy in the second near-infrared window. *J Am Chem Soc*. 2014;136(4):15684–15693. doi:10.1021/ja508641z

International Journal of Nanomedicine Dovepress

Publish your work in this journal

The International Journal of Nanomedicine is an international, peer-reviewed journal focusing on the application of nanotechnology in diagnostics, therapeutics, and drug delivery systems throughout the biomedical field. This journal is indexed on PubMed Central, MedLine, CAS, SciSearch®, Current Contents®/Clinical Medicine, Journal Citation Reports/Science Edition, EMBase, Scopus and the Elsevier Bibliographic databases. The manuscript management system is completely online and includes a very quick and fair peer-review system, which is all easy to use. Visit http://www.dovepress.com/testimonials.php to read real quotes from published authors.

Submit your manuscript here: https://www.dovepress.com/international-journal-of-nanomedicine-journal